Pure Appl. Geophys. 174 (2017), 3467–3478

DOI 10.1007/s00024-016-1424-7

Pure and Applied Geophysics

Azimuthal Dependence of the Ground Motion Variability from Scenario Modeling of the 2014 Mw6.0 South Napa, California, Earthquake Using an Advanced Kinematic Source Model

F. Gallovič[1]

Abstract—Strong ground motion simulations require physically plausible earthquake source model. Here, I present the application of such a kinematic model introduced originally by Ruiz et al. (Geophys J Int 186:226–244, 2011). The model is constructed to inherently provide synthetics with the desired omega-squared spectral decay in the full frequency range. The source is composed of randomly distributed overlapping subsources with fractal number-size distribution. The position of the subsources can be constrained by prior knowledge of major asperities (stemming, e.g., from slip inversions), or can be completely random. From earthquake physics point of view, the model includes positive correlation between slip and rise time as found in dynamic source simulations. Rupture velocity and rise time follows local S-wave velocity profile, so that the rupture slows down and rise times increase close to the surface, avoiding unrealistically strong ground motions. Rupture velocity can also have random variations, which result in irregular rupture front while satisfying the causality principle. This advanced kinematic broadband source model is freely available and can be easily incorporated into any numerical wave propagation code, as the source is described by spatially distributed slip rate functions, not requiring any stochastic Green's functions. The source model has been previously validated against the observed data due to the very shallow unilateral 2014 Mw6 South Napa, California, earthquake; the model reproduces well the observed data including the near-fault directivity (Seism Res Lett 87:2–14, 2016). The performance of the source model is shown here on the scenario simulations for the same event. In particular, synthetics are compared with existing ground motion prediction equations (GMPEs), emphasizing the azimuthal dependence of the between-event ground motion variability. I propose a simple model reproducing the azimuthal variations of the between-event ground motion variability, providing an insight into possible refinement of GMPEs' functional forms.

Key words: 2014 Mw6 South Napa earthquake, kinematic strong ground motion modeling, scenario modeling, between-event ground motion variability, single-station sigma, directivity.

1. Introduction

Strong ground motion simulations require physically plausible earthquake source model. The method must be able to provide omega-square source spectrum in a broad frequency range, as it is commonly observed in the real data. Moreover, the model must be compatible with basic characteristics observed in earthquake source studies of real events and with properties suggested by earthquake source dynamics.

In general, in strong ground motion modeling, kinematic models are preferred to the dynamic ones for much better numerical efficiency. Here, I apply one of the kinematic methods, which is based on the evaluation of the representation theorem (Aki and Richards 2002). The source process is prescribed in terms of spatial–temporal evolution of slip along the fault. Numerically, the fault is discretized and the representation integral is substituted by a sum, so that the finite extent source is represented as a coherent superposition of point sources distributed regularly along the fault with spatial spacing small enough to avoid numerical problems in the integration. I note that this approach differs from the so-called composite modeling, which is based on the assumption that the modeled event can be described as a discrete sequence of individually rupturing subevents that are treated as point sources (e.g., Zeng et al. 1994). Another viable approach to strong motion modeling is a hybrid combination of the latter two methods (e.g., Graves and Pitarka 2010; Gallovič and Brokešová 2007). However, the disadvantage of such combination is the need for crossover filtering of the synthetics simulated by the two techniques, which is typically performed ad hoc (Ameri et al. 2012).

[1] Department of Geophysics, Faculty of Mathematics and Physics, Charles University in Prague, V Holešovičkách 2, 180 00 Praha 8, Czech Republic. E-mail: gallovic@karel.troja.mff.cuni.cz

In the present paper, I utilize a method introduced by Ruiz et al. (2011), hereafter denoted as Ruiz Integral Kinematic (RIK) model, with some minor modifications. It has been recently applied to the broadband modeling of the observed velocity waveforms written by the 2014 Mw6 South Napa earthquake (Gallovič 2016). I first explain the basic characteristics of the source model, taking newly into account random variations of the rupture speed along the fault. I employ full wavefield Green's functions calculated in a 1D velocity model and perform scenario simulations to predict possible variability of ground motions due to varying hypocenter location, mean rupture speed and slip distribution. I compare the results with empirical ground motion prediction equations (GMPEs) and explore spatial (azimuthal) distribution of the simulated ground motion variability. In recent GMPEs, two components of ground motion variability are distinguished (see, e.g., Causse and Song 2015): the within-event variability (due to path and site effects for a given event) and the between-event variability (due to varying properties of the source process). Our scenario-based variability is thus compared with the between-event standard deviations of the empirical GMPEs.

Eventually, I propose a simple model that reproduces the azimuthal variability of the between-event ground motion variability. This model could be employed to refine GMPEs' functional forms.

2. RIK Source Model Description

The RIK model has been developed by Ruiz et al. (2011) for earthquake ground motion simulations to provide omega-squared spectral decay at high frequencies. It utilizes the representation integral in the full frequency range (no composite modeling needed). In Gallovič (2016), some simplifications and minor modifications of the method have been introduced, such as taking into account the depth dependence of the rupture velocity. I additionally introduce random variations of the rupture speed as discussed further.

The RIK model is composed of randomly distributed overlapping circular subsources with fractal number-size distribution with dimension $D = 2$, which is considered also in other kinematic source models (e.g., Zeng et al. 1994; Gallovič and Brokešová 2007). Kinematic properties (including the rupture propagation) are prescribed individually to each of the subsources, and thus each subsource is characterized by its own slip rate function distribution along its areal extent. The total slip rates of the RIK model are eventually evaluated on a regular discretization grid along the fault by summing up slip rate contributions from all the subsources.

In particular, I consider that radii of the subsources, R, are integer fractions of the fault width W, i.e., $R = W/n$. For the present number-size distribution, the number of subsources at level n is then $2n - 1$. The subsources are distributed randomly along the fault. In the scenario modeling, I consider uniform distribution, but in the real data modeling one can use slip distribution obtained from inversion of low-frequency data to constrain the subsource distribution (see Gallovič 2016).

The individual subsources have slip distributions corresponding to the crack model, i.e.,

$$\begin{aligned} \Delta u^R(\rho) &= c\sqrt{R^2 - \rho^2} \quad \text{if } \rho < R; \\ \Delta u^R(\rho) &= 0 \quad \text{otherwise}, \end{aligned} \tag{1}$$

where ρ is the distance from the subsource center. The constant of proportionality c in (1) is determined so that the total seismic moment (i.e., sum of seismic moments of all the subsources) equals the prescribed scalar seismic moment M_0. This fractal decomposition of the source model implies that the slip decays as k^{-2} at high wavenumbers k (Andrews 1980; Gallovič and Brokešová 2007). It also implies physically plausible k^{-1} spectral decay of the stress distribution (Andrews 1980).

The rupture is assumed to propagate in the form of a slip pulse of width L_0 with the Brune's pulse (Brune 1970) as the slip rate function. If rise time were constant, the source spectrum would decay as omega-squared only up to the reciprocal of the rise time, decaying then faster due to the low-pass filtering effect of the slip rate function. To correct for this, Bernard et al. (1996) introduced the concept of the k-dependent rise time (see also Gallovič and Brokešová 2007). In the RIK model with subsources of varying sizes, the rise time is considered to depend on subsource radius R as

$$\tau(R) = \tau_{\max} = aL_0/v_r \quad \text{if } 2R > L_0; \qquad \tau(R) = a(2R)/v_r \quad \text{otherwise}, \tag{2}$$

where a is a free parameter (of the order of 1). Rupture speed v_r follows the S-wave velocity profile, keeping the rupture speed to S-wave velocity ratio constant. This way, one avoids too fast (possibly supershear) rupture propagation close to the surface and thus enhanced source radiation. The rise time dependence on the subsource radii (Eq. 2) also implies a positive spatial correlation between the slip and the rise time as it is observed in dynamic rupture simulations (e.g., Schmedes et al. 2010).

Ruiz et al. (2011) introduced a concept of small- and large-scale rupture fronts to decrease the coherency of the rupture front. Gallovič (2016) showed that taking this feature into account led to improved fit including better capture of the azimuthal variability of the observed data. In addition, I consider also random variations of the rupture speed following a k^{-1} distribution. The rupture times are numerically evaluated using the solver of the eikonal equation by Podvin and Lecomte (1991), so that the causality of the rupture front is satisfied.

3. Source and Velocity Model

The South Napa earthquake occurred on 24 August 2014 at 10:20:44 UTC in California, 6 km NW of American Canyon and 9 km SW of Napa (Brocher et al. 2015). For this earthquake, many high-quality recordings were obtained by stations located at near-fault distances (see Fig. 1).

Gallovič (2016) presents a slip inversion of the South Napa earthquake utilizing the method by Gallovič et al. (2015) and near-fault stations (Fig. 1). The model is in agreement with other models published so far (Dreger et al. 2015; Ji et al. 2015; Melgar et al. 2015; Wei et al. 2015), showing a unilateral north–northwest rupture propagation toward the city of Napa, having significant asperity at shallow depths (<5 km) with longer rise times at the place where 40–46 cm slip was observed at the surface (Brocher et al. 2015). The rupture propagation direction has been also recently inferred from the spatial distribution of peak ground motions by Convertito et al. (2016). I adopt the fault geometry from the RIK model parameters from Gallovič (2016); see Fig. 1.

For the wave propagation modeling, I use a modification of the 1-D layered velocity model GIL7 (Stidham et al. 1999), with two additional layers with subsurface velocity representing hard-rock site properties (see Table S2 in Gallovič 2016). Full wavefield Green's functions (GFs) are calculated using the discrete wavenumber technique (Axitra code, Bouchon 1981; Coutant 1989) in the frequency range 0–10 Hz. No stochastic GFs are used throughout the whole study.

4. Results

4.1. Ground Motion Simulation for the South Napa Earthquake Model

I perform simulation of the ground motion distribution considering the RIK model parameters from Gallovič (2016). In particular, the distribution of the subsources of the RIK model is constrained by the slip model from the low-frequency data inversion by Gallovič (2016). The mean rupture velocity is considered also as 0.8 times the local rupture velocity. I only add random variations to the rupture speed with standard deviation equal to ¼ of the local rupture speed. This leads to a modest distortion of the otherwise coherent rupture front obtained if a constant rupture velocity was considered.

For the comparison between synthetic and observed data, see Gallovič (2016). I concentrate on the prediction of spatial ground motion distribution for this model, carrying out the simulations at a regular distribution of phantom stations (see Fig. 1). The red points in Fig. 2a, b show the simulated PGV and PGA values, respectively, as a function of the Joyner–Boore distance. The plots are complemented by the real data peak values and GMPEs of Boore et al. (2014). The latter represents all available GMPEs for California, as they provide very similar attenuation curves in the present case (see Fig. 4 of Brocher et al. 2015). Note that the real data overshoot the mean GMPE curves, especially in terms of PGV, while at larger distance the observed values are smaller than those predicted by GMPEs. This

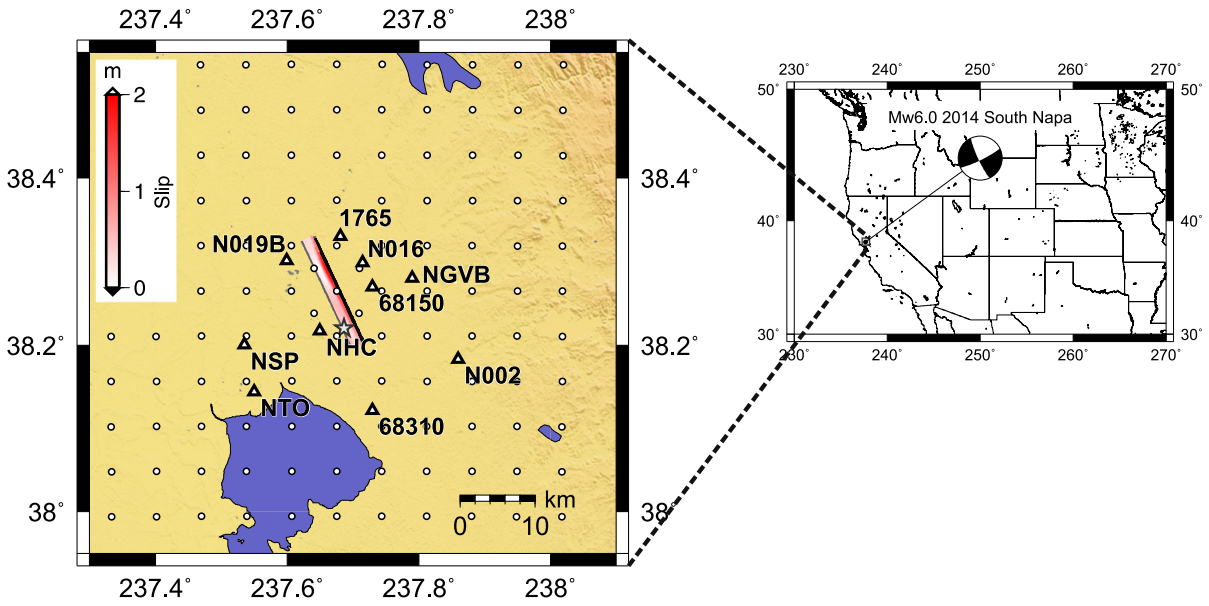

Figure 1

Left distribution of near-fault stations (*triangles*) that recorded the 2014 South Napa earthquake. *Box* represents the surface projection of the fault with superimposed slip distribution adopted from Gallovič (2016). *Star* denotes the nucleation point of the event. *Small circles* show the position of the phantom stations considered in the scenario simulations. *Right* map of USA showing the location of the area under study

behavior, which results in a seemingly stronger attenuation with distance than suggested by the GMPE curves, is well captured by the strong motion simulations. This particular behavior can be ascribed to the very shallow location of the major asperity, which is a distinct feature of this particular event. Figure 2c, d shows the map views of the simulated PGV and PGA values, respectively, with sensible amplification in the NE direction due to the directivity effect. This is in agreement with the shape of the ShakeMap produced by the US Geological Survey (see http://earthquake.usgs.gov/earthquakes/shakemap/nc/shake/72282711/or Gallovič 2016).

4.2. *Scenario Modeling*

In deterministic seismic hazard assessment, one is typically interested in strong ground motion prediction for a hypothetical earthquake on an assumed fault. Typically, the mechanism and geometry of a causative fault can be constrained a priori with some epistemic uncertainty. However, the details of the rupture process, such as the position of the nucleation point, asperity, or rupture velocity, are generally not known in advance, representing a source of aleatory uncertainty. In such a case, scenario simulations are performed to take into account possible variations of the source parameters.

To estimate this (between-event) variability related to the a priori unknown rupture scenario, I assume the following variations of the source parameters: two ratios between the mean rupture speed and S-wave velocities (0.6 and 0.8), six positions of the nucleation point on the fault and three slip distributions (i.e., realizations of the random subsource distribution); see Fig. 3a. In addition, I consider horizontally mirrored models to improve the symmetry of the simulated scenarios. Considering all combinations of the rupture parameters, I thus generate 72 rupture scenarios in total. For each of the scenarios, I consider a unique distribution of the rupture speed variations. Figure 3b shows examples of three of the source scenarios in terms of rupture evolution snapshots. The rupture propagation is characterized by similar complexity as the model used for modeling the observed data.

Figure 4 displays the resulting PGV and PGA values picked from the simulated seismograms (red

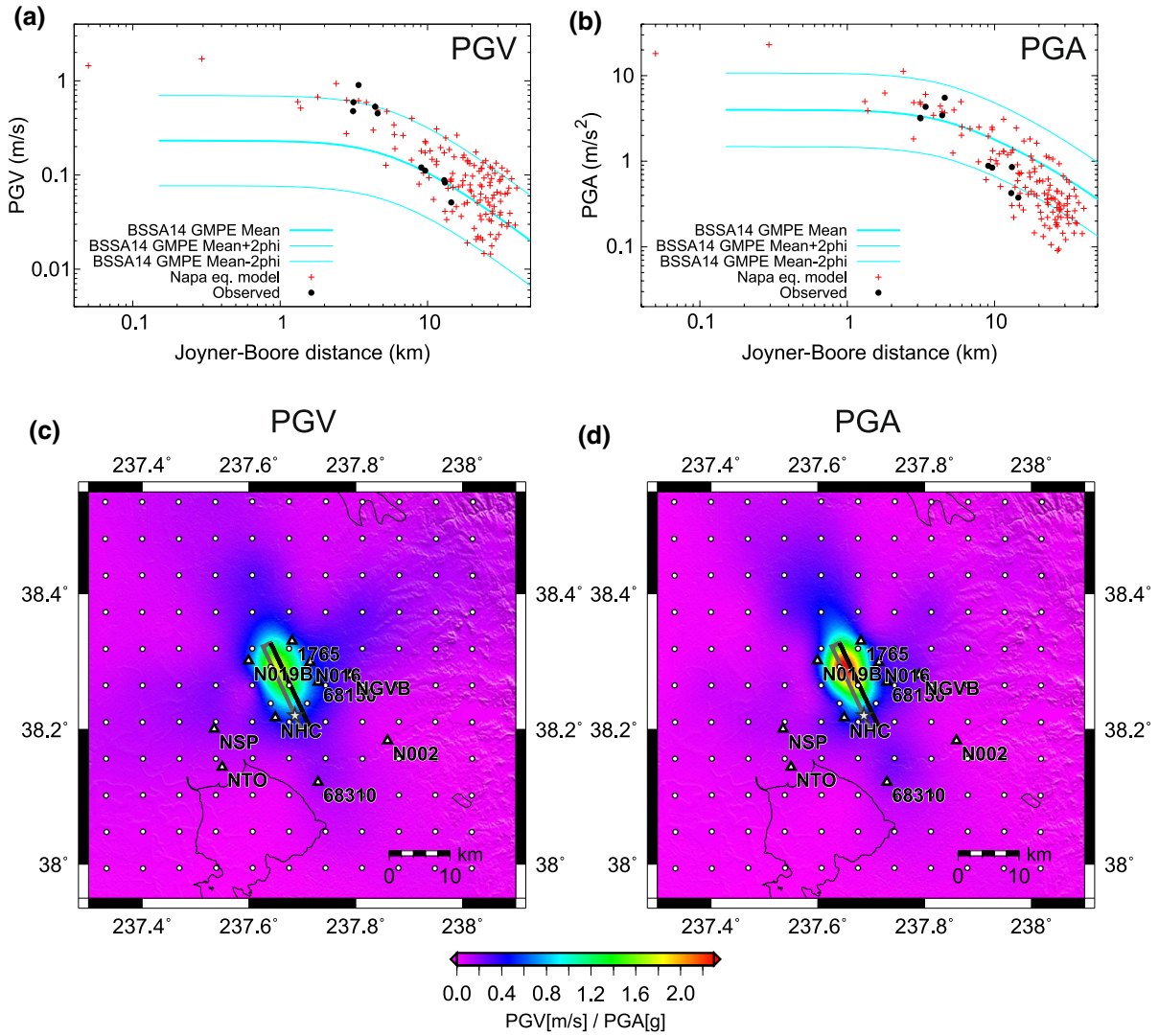

Figure 2

a Comparison between the simulated (*red points*) and observed (*black points*) PGV values collected from all the real and phantom stations (Fig. 1). *Lines* represent the mean (*thick*) and mean ± 2ϕ (thin) of the GMPE (Boore et al. 2014), where ϕ is the within-event standard deviation. **b** Same as (**a**) but for PGA. **c** Map view of the simulated PGV values interpolated from all the real and phantom stations (*triangles* and *circles*, respectively). The interpolation is performed using generic mapping tools (code surface) assuming minimum curvature solution. **d** Same as (**c**) but for PGA

dots) against the Joyner–Boore distance. For reference, the GMPEs and real data are plotted as well. The scatter of the simulated values is relatively large, having standard deviation of approximately 0.8 (in natural log units). This value is larger than the standard deviation of the GMPEs (including both within- and between- event variability), which is approximately 0.6–0.65 and roughly constant for the distance range considered (Boore et al. 2014). Most likely adding complexity to the path and/or site effects to include the scattering effect in the modeling would reduce the simulated ground motion variability (Imperatori and Mai 2012; Sato et al. 2012). I also note that to some extent this discrepancy could be ascribed to the abundant number of earthquake scenarios and seismic station density considered in

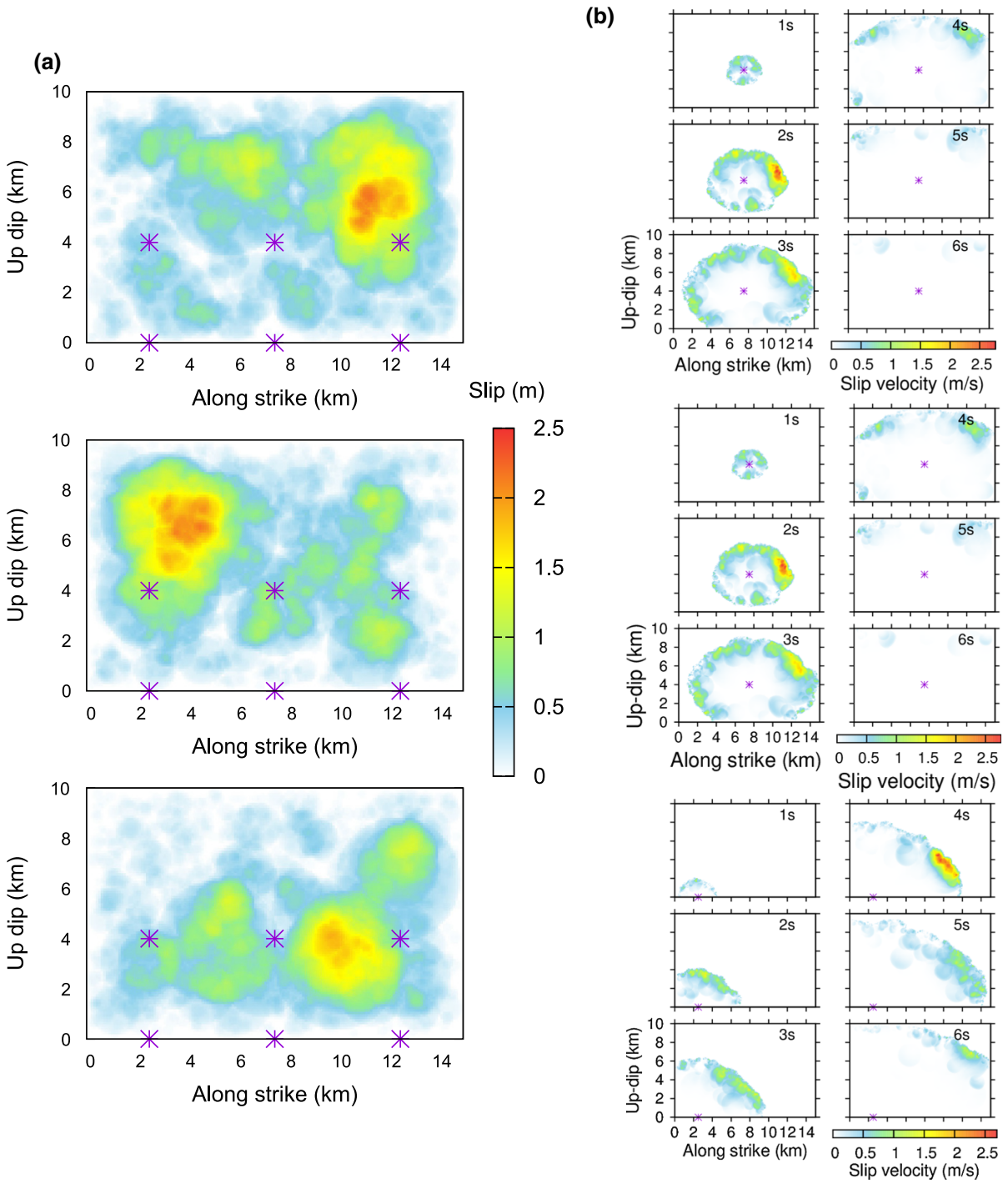

Figure 3
Setup of the scenario modeling. **a** Three slip distribution models with considered positions of nucleation points (*stars*). **b** Three examples of the rupture propagation scenarios plotted in terms of slip rate snapshots. *Stars* represent actual nucleation point positions of the particular models

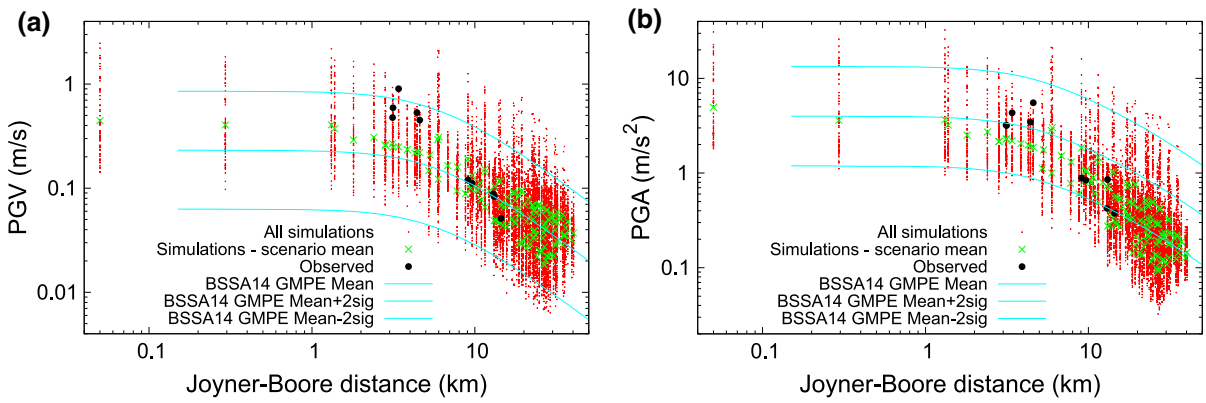

Figure 4
Results of the scenario simulations. *Red points* are simulated PGV (**a**) and PGA (**b**) from all scenarios and stations. *Lines* represent the mean (*thick*) and mean $\pm$ 2σ (*thin*), where σ is the complete standard deviation of the GMPE (Boore et al., 2014) including within- and between-event variabilities. *Green crosses* show the mean values over scenarios for each of the stations considered

the simulations, which exceeds a standard number of observations in real cases, so that scarcer real observations might not capture all systematic features of the earthquake ground motions as suggested by the simulations (see also further). Figure 4 shows also mean values of the peak values evaluated over all the scenarios at each station. The mean peak values have smaller scatter (with log standard deviation $\sim$0.4). They decay slightly faster with distance (especially in terms of PGA), which resembles the faster decay of the observed data. In the case of modeling the real data, I have ascribed it to the superficial character of the slip distribution. In this case, I cannot use this argument solely, although there are a larger number of models having shallower slip (see Fig. 3). The 1D velocity model seems to attenuate the seismic waves more strongly than that suggested by the empirical data (GMPEs). It is also possible that the adopted velocity model lacks some superficial structure that would enhance the seismic waves at larger distances.

Figure 5 shows the spatial distribution of the simulated PGV and PGA values in terms of their mean and standard deviations (in natural log units). The mean values have elongated shape following the geometry of the fault. A minor effect of the radiation pattern can be also seen, being expressed by the cross-like character of the peak-value maps. In terms of the ground motion variability, the simulations suggest spatially inhomogeneous standard deviation (also called single-station between-event sigma) ranging from approximately 0.3 to 0.9. Indeed, the corresponding maps in Fig. 5 have a fan-like shape with the largest values located above the fault and along the directions of the fault. Both of them are related to the directivity effect, which is mostly pronounced in the up-dip and along-fault directions. Indeed, the variability is lowest in the directions perpendicular to the fault, where the ground motions are not much affected by the direction, in which the rupture front propagates. The root mean square of the variability over all the stations is 0.6 for both PGV and PGA.

For four selected phantom stations depicted in Fig. 5, I show the histograms of the simulated PGA values in Fig. 6. The histograms have various shapes, resembling normal distribution (e.g., station 75). In some cases (stations 82 and 52), they indicate a bimodal character. This bimodal shape occurs generally at stations lying in the along-strike direction. They are perhaps imprints of the significant difference between the peak values simulated in scenarios with predominantly forward and backward directivity directions.

The plots in Fig. 6 show also PGA values obtained considering the source model used to simulate the observed data (crosses). They fall within the histograms from the scenario simulations. However, one can see that the values obtained for the constrained source model do not fall to the same part of the histograms for various stations; in some cases,

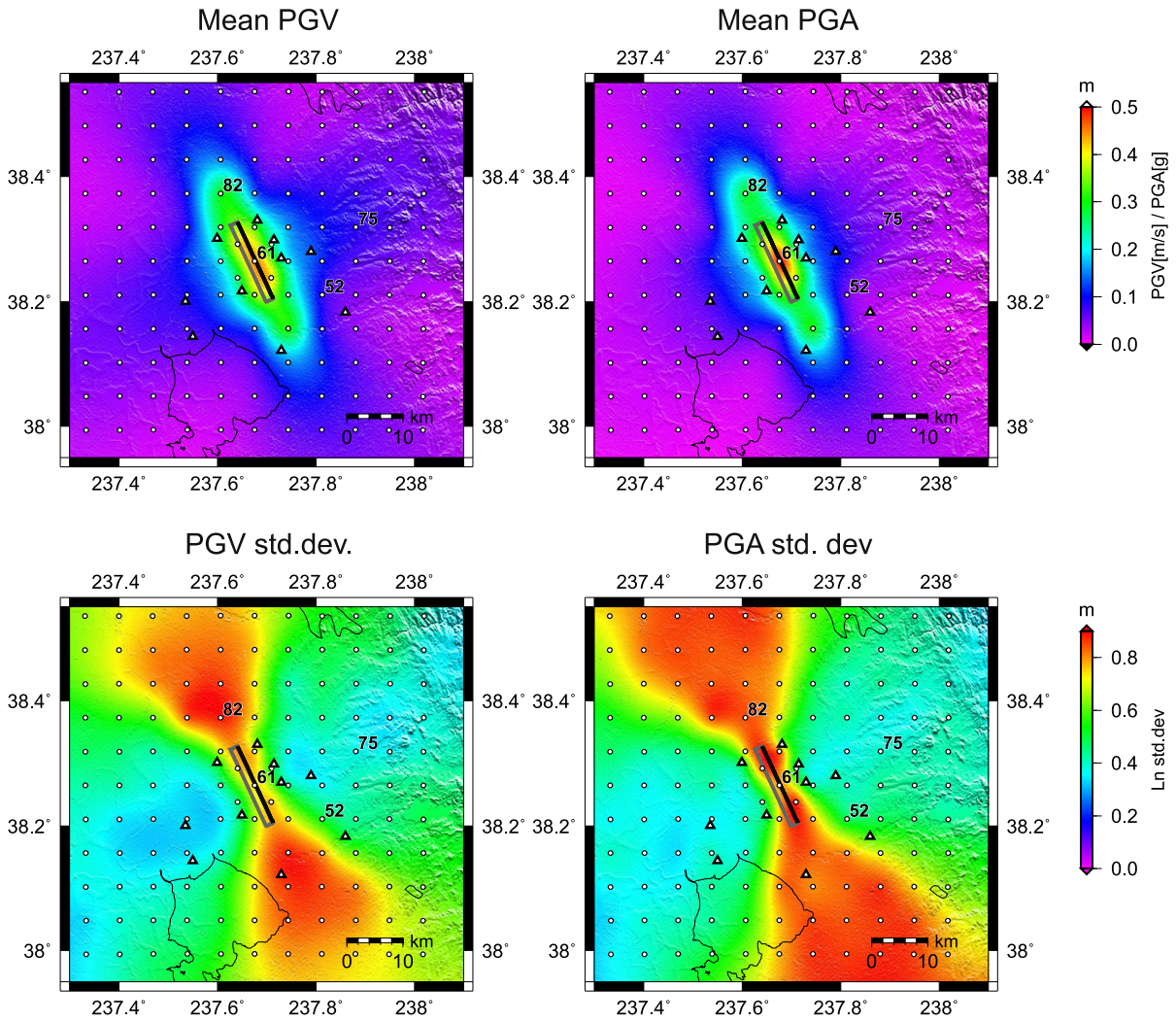

Figure 5
Results of the scenario simulations plotted in terms of the mean values of PGA and PGV evaluated over all the scenarios and their variability. *Triangles* and *small circles* denote the real and phantom stations, respectively. For the numbered phantom stations, Fig. 6 shows the histograms of the PGA values

they fall at the margin of the distribution (stations 75 and 61), while in other cases they are located approximately at their centers (stations 82 and 52).

4.3. Factorization of the Ground Motion Variability

Figure 7 shows the simulated single-station between-event standard deviations of PGA and PGV (in natural logarithm) plotted as a function of angle from the fault strike assuming fault distances larger than the fault length (>15 km). The standard deviations exhibit a distinct azimuthal dependence as already observed in Fig. 5. Their values range from 0.3 to 0.9 with root-mean-square value (over all stations) of 0.6.

In the present simulations, the ground motion variability arises from variations of nucleation point, slip distribution and rupture velocity. In particular, the variability of the nucleation point position, which controls the directivity effect, is usually considered as the major source of the variability with pronounced azimuthal dependence. I aim to factorize the ground

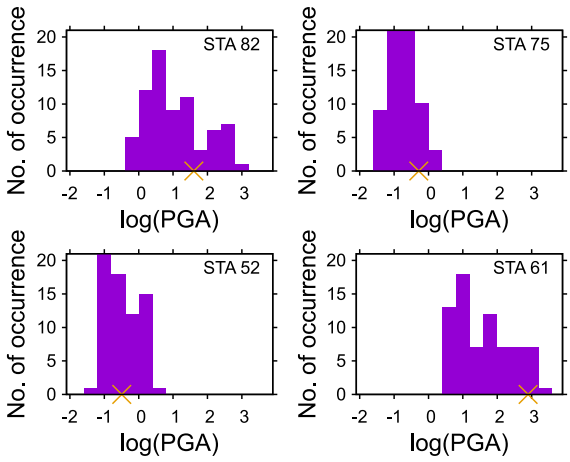

Figure 6
Histograms of (natural log) the PGA values corresponding to the numbered phantom stations in Fig. 5. *Crosses* denote the values obtained from the simulations of the observed data by Gallovič (2016)

motion variability into factors related to directivity and the remaining (azimuthally independent) scenario components.

I consider that the simulated peak value $P(\theta,l,\alpha,i,r)$ depends on the station azimuth θ (measured from north), distance r, nucleation point position l (normalized by the rupture length, thus ranging from 0 to 1), ratio α between the rupture velocity v_r and S-wave speed c ($\alpha = \frac{v_r}{c}$), and all other source parameters varied in the scenario simulations altogether denoted as i. I assume that $P(\theta,l,\alpha,i,r)$ can be partitioned into factors dependent exclusively on θ, l, α, i, r and some multiplicative constant C, i.e.,

$$P(\theta,l,\alpha,i,r) = C(\theta)A(\theta,l,\alpha)S(i)R(r), \qquad (3)$$

where $R(r)$ denotes the distance dependence, $A(\theta,l,\alpha)$ directivity function, $S(i)$ the scenario variability and $C(\theta)$ includes all the remaining source and site properties, which are independent or almost independent of the particular rupture scenario, such as seismic moment, radiation pattern and site effect. To particularly highlight the dependence of C on the radiation pattern, I explicitly depict its dependence on θ. The logarithm of Eq. (3) then reads

$$\log P(\theta,l,\alpha,i,r) = \log C(\theta)R(\mathrm{r}) + \log A(\theta,l,\alpha) + \log S(i). \qquad (4)$$

The expected value (mean) of Eq. (4) over scenario parameters l, α and i for each station can be written as

$$\log P(\theta,l,\alpha,i,r)_{l,\alpha,i}(\theta,r) = \log C(\theta)R(r) + \log A(\theta,l,\alpha)_{l,\alpha} + \log S(i)_i, \qquad (5)$$

and the corresponding variance reads (after simple algebra)

$$\begin{aligned}\mathrm{var}(\log P(\theta,l,\alpha,i,r))_{l,i,\alpha}(\theta,r) &= \log^2 P(\theta,l,i,r)_{l,\alpha,i} \\ &\quad - \log P(\theta,l,i,r)^2_{l,\alpha,i} \\ &= \mathrm{var}(\log A(\theta,l,\alpha))_{l,\alpha}(\theta) \\ &\quad + \mathrm{var}(\log S(i))_i. \end{aligned} \qquad (6)$$

Note that Eq. (6) suggests that the variance does not depend on any constants which are scenario independent, including radiation pattern and the distance. This makes Eq. (6) ideal to discriminate the effect of the nucleation point position (directivity) from the complete ground motion variability, in contradiction to the more complicated Eq. (5).

I develop a simple model to fit the azimuthal dependence of the ground motion variability (Fig. 7). The model is based on a narrow fault approximation with randomly located nucleation points and randomly chosen rupture velocities. I start assuming a unilateral rupture radiating an omega-squared source spectrum with corner frequency F_c being proportional to αC_d, where C_d is the directivity coefficient (Ben-Menahem 1961).

$$C_d(\theta,\alpha) = \frac{1}{1-\alpha\cos(\theta-\phi)}, \qquad (7)$$

where ϕ is the direction of the dominant rupture propagation (i.e., fault strike). In such a case, the high-frequency acceleration spectral plateau is proportional to $M_0 F_C^2(\theta,\alpha)$, and thus A reads

$$\log A(\theta,l=0,\alpha) = \log \alpha^2 C_d^2(\theta,\alpha). \qquad (8)$$

Since theoretical (Bernard et al. 1996; Gallovič and Burjánek 2007), empirical (Somerville et al. 1997; Pacor et al. 2016) and experimental (Day et al. 2008) studies suggest that the high-frequency directivity likely attains weaker azimuthal dependence than suggested by Eq. (8), I relax the exponent value in Eq. (8) and assume a general power n, i.e.,

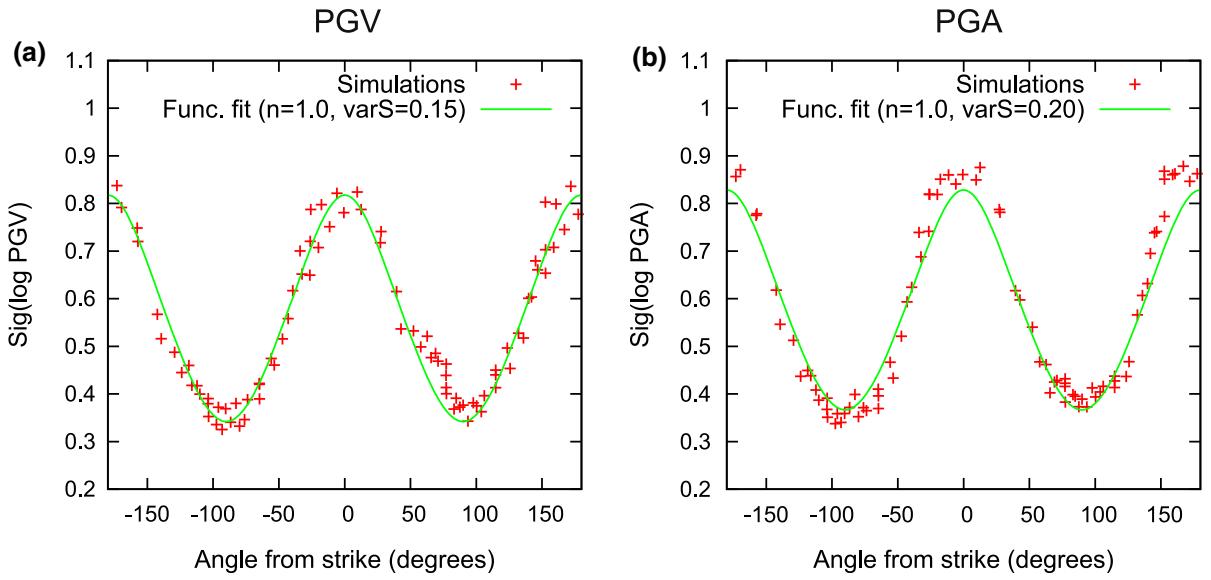

Figure 7
Factorization of the ground motion variability. Standard deviation of the PGV (**a**) and PGA (**b**) values (*red pluses*) plotted as a function of the station angle from the fault strike considering epicentral distances larger than 15 km. The values are fitted by a theoretical curve (Eq. 11) with values specified in the legend

$$\log A(\theta, l=0, \alpha) = \log \alpha^2 C_d^n(\theta, \alpha). \tag{9}$$

Note that $n = 1$ corresponds to the Haskell model that is typically utilized in studies of directivity of earthquakes.

Considering that the rupture is not unilateral, the directivity dependence needs to be modified. Assuming that the ground motions at high frequencies sum incoherently, one gets

$$\log A(\theta, l, \alpha) = \log \alpha^2 \sqrt{\left((1-l)C_d^n(\theta,\alpha)\right)^2 + \left(lC_d^n(180^\circ - \theta, \alpha)\right)^2}. \tag{10}$$

Putting Eqs. (7) and (9) into Eq. (10) yields

$$\log A(\theta, l, \alpha) = \log \alpha^2 \sqrt{\frac{(1-l)^2}{(1-\alpha\cos\theta)^{2n}} + \frac{l^2}{(1+\alpha\cos\theta)^{2n}}}. \tag{11}$$

Equation (11) is then put into Eq. (6) and the variance of $\log(A)$ over nucleation point positions l and rupture to S-wave speed ratio α in Eq. (11) is calculated numerically, assuming a uniform distribution of l and α in the range 0–1 and 0.6–0.8, respectively.

To fit the azimuthal dependence of the simulated standard deviations (Fig. 7), I have optimized the free parameters n and the azimuthally independent $var(\log S(i))_i$. Figure 7 then shows this optimized theoretical functions and their parameters. One can see that the theoretical model fits the simulated standard deviations very well (Fig. 7) despite their simplicity.

The parameter values found suggest that the between-event variability is dominated by the directivity effect in the present simulations. If the nucleation point variability was neglected, the variability would be as low as $var(\log S(i))_i = 0.2$. Taking into account the randomness of the hypocenter location increases the variability by ~ 0.2 in the fault-perpendicular direction and ~ 0.6 in the along-strike direction, the inferred value of the exponent $n = 1$ corresponds to the classical Haskell model.

5. Discussion and Conclusions

In this study, I have employed an advanced broadband kinematic source model originally introduced by Ruiz et al. (2011). It is characterized by k^{-2} slip distribution and k-dependent rise time, providing correctly omega-squared source spectrum in the full frequency range (see Gallovič 2016). I have introduced several minor modifications, such as dependence of the rupture

speed on the 1D velocity profile to avoid too fast (possibly supershear) rupture propagation close to the surface. I have also included random variations of the rupture speed to distort the otherwise too coherent rupture front.

Gallovič (2016) validated the approach against near-fault high-quality recordings of the 2014 Mw6 South Napa earthquake in a broad frequency range (0.05–5 Hz). Full wavefield Green's functions calculated in a 1D velocity model roughly corresponding to a hard-rock site are taken into account in the whole frequency range (no stochastic Green's functions were utilized). Gallovič (2016) shows that the model correctly reproduces the major characteristics of the observed data, including their peak values and broad directivity pulses in the velocity waveforms.

I extend the previous study performing scenario simulations for the South Napa causative fault in the frequency range of 0–10 Hz. To this end, I have generated 72 source models with varying rupture speed, nucleation point position and slip distribution to evaluate between-event variability of the ground motions. The resulting maps of the average peak motions have an elongated shape due to the finite extent of the fault. PGA and PGV values decay slightly more rapidly with increasing distance than suggested by the empirical GMPEs (Boore et al. 2014). The variability of the ground motions (in terms of single-station between-event standard deviation) shows a peculiar fan-like shape with the largest values in the along-strike directions. I ascribe this to the effect of directivity, which is most pronounced in those directions. The directivity effect is also imprinted in the histograms of the peak values at stations in the along-strike directions, having rather a bimodal character.

The simulated single-station between-event standard deviations range from 0.3 to 0.9 with root-mean-square value (over all stations) of 0.6, which is larger than the between-event standard deviations of GMPEs (0.3–0.4, see the review by Causse and Song, 2015). I assume that, in reality, scattering of seismic waves can lead to a reduction of the ground motion variability especially at larger distances as suggested by simulation studies (e.g., Imperatori and Mai 2012; Sato et al. 2012).

Although the present application utilizes just a 1D velocity model to evaluate ground motions, the source model can be easily implemented in any code simulating wave propagation in generally 3D media. In terms of scenario simulations, I expect that the 3D model would mainly affect the mean ground motions and perhaps also the variability at further distances in directions perpendicular to the fault. Contrarily, I suppose that close to the fault and in the along-strike directions, the source effect plays a dominant role in controlling the between-event ground motion variability.

I note that the standard GMPEs take into account only distance dependence of the observed motion, neglecting any possible azimuthal dependence of the between-event ground motion variability as suggested by the simulations. The latter may thus help to introduce new types of functional forms of GMPEs that would take into account the azimuthal dependence of the ground motion variability due to the source effect. For this purpose, I have introduced a simple model that captures the azimuthal dependence of the between-event ground motion variability. I note that the present paper complements recent studies of Vyas et al. (2016) and Imtiaz et al. (2015), who analyze the within-event variability in ground motion simulations, providing thus insight into the total ground motion variability.

The code for generation slip rate functions using the RIK model is freely available for general applications from the GitHub repository at https://github.com/fgallovic/RIKsrf.

Acknowledgements

I acknowledge the reviews provided by the two anonymous reviewers who helped to improve the manuscript. Accelerometric data were downloaded from the freely available online repository Center for Engineering Strong Motion Data (CESMD, http://strongmotioncenter.org). Map figures were prepared using the Generic Mapping Tools package (http://www.soest.hawaii.edu/gmt/). Financial support: Grant Agency of Czech Republic 14-04372S.

References

Aki, K., & Richards, P. G. (2002). *Quantitative seismology*. Sausalito, California: University Science.

Ameri, G., Gallovič, F., & Pacor, F. (2012). Complexity of the Mw6.3 2009 L'Aquila (Central Italy) earthquake: 2. Broadband strong-motion modeling. *Journal Geophysical Research, 117*, B04308. doi:10.1029/2011JB008729.

Andrews, D. J. (1980). A stochastic fault model: 1. static case. *Journal Geophysical Research, 85*, 3867–3877.

Ben-Menahem, A. (1961). Radiation of seismic surface waves from finite moving sources. *Bulletin of the Seismological Society of America, 51*, 401–435.

Bernard, P., Herrero, A., & Berge, C. (1996). Modeling directivity of heterogeneous earthquake ruptures. *Bulletin of the Seismological Society of America, 86*, 1149–1160.

Boore, D. M., Stewart, J. P., Seyhan, E., & Atkinson, G. M. (2014). NGA-West 2 equations for predicting PGA, PGV, and 5%-damped PSA for shallow crustal earthquakes. *Earthquake Spectra, 30*, 1057–1085.

Bouchon, M. (1981). A simple method to calculate Green's functions for elastic layered media". *Bulletin of the Seismological Society of America, 71*, 959–971.

Brocher, T. M., et al. (2015). The M 6.0 24 August 2014 South Napa Earthquake". *Seismological Research Letters, 86*, 309–326.

Brune, J. N. (1970). Tectonic stress and the spectra of seismic shear waves from earthquakes. *Journal Geophysical Research, 75*, 4997–5009.

Causse, M., & Song, S. G. (2015). Are stress drop and rupture velocity of earthquakes independent? Insight from observed ground motion variability. *Geophysical Research Letters, 42*, 7383–7389.

Convertito, V., De Matteis, R., & Emolo, A. (2016). Investigating Triggering of the Aftershocks of the 2014 Napa Earthquake. *Bulletin of the Seismological Society of America, 106*, 2063–2070.

Coutant, O. (1989). *Program of numerical simulation AXITRA", research report*. Grenoble, France: Lab. de Geophys. Interne et Tectonophys.

Day, S. M., Gonzalez, S. H., Anooshehpoor, R., & Brune, J. N. (2008). Scale-model and numerical simulations of near-fault seismic directivity. *Bulletin of the Seismological Society of America, 98*(3), 1186–1206.

Dreger, D. S., Huang, M.-H., Rodgers, A., Taira, T., & Wooddell, K. (2015). Kinematic finite-source model for the 24 August 2014 South Napa, California, earthquake from joint inversion of seismic, GPS and InSAR data. *Seismological Research Letters, 86*, 327–334.

Gallovič, F. (2016). Modeling velocity recordings of the Mw6.0 South Napa, California, earthquake: unilateral event with weak high-frequency directivity. *Seismological Research Letters, 87*, 2–14.

Gallovič, F., & Brokešová, J. (2007). Hybrid k-squared source model for strong ground motion simulations: introduction. *Physics of the Earth and Planetary Interiors, 160*, 34–50.

Gallovič, F., & Burjánek, J. (2007). High-frequency directivity in strong ground motion modeling methods. Annals of Geophysics *50*(2), 203–211.

Gallovič, F., Imperatori, W., & Mai, P. M. (2015). Effects of three-dimensional crustal structure and smoothing constraint on earthquake slip inversions: case study of the Mw6.3 2009 L'Aquila earthquake. *Journal Geophysical Research, 120*, 428–449.

Graves, R. W., & Pitarka, A. (2010). Broadband ground-motion simulation using a hybrid approach. *Bulletin of the Seismological Society of America, 100*, 2095–2123.

Imperatori, W., & Mai, M. P. (2012). Broad-band near-field ground motion simulations in 3-dimensional scattering media. *Geophysical Journal International, 192*(2), 725–744.

Imtiaz, A., Causse, M., Chaljub, E., & Cotton, F. (2015). Is ground-motion variability distance-dependent? Insight from finite-source rupture simulations. *Bulletin of the Seismological Society of America, 105*, 950–962.

Ji, Ch., Archuleta, R. J., & Twardzik, C. (2015). Rupture history of 2014 Mw 6.0 South Napa earthquake inferred from near fault strong motion data and its impact to the practice of ground strong motion prediction. *Geophysical Reseach Letters, 42*, 2149–2156.

Melgar, D., Geng, J., Crowell, B. W., Haase, J. S., Bock, Y., Hammond, W. C., et al. (2015). Seismogeodesy of the 2014 Mw6.1 Napa earthquake, California: rapid response and modeling of fast rupture on a dipping strike-slip fault. *Journal of Geophysical Research: Solid Earth, 120*, 5013–5033.

Pacor, F., Gallovič, F., Puglia, R., Luzi, L., & D'Amico, M. (2016). Diminishing high-frequency directivity due to a source effect: empirical evidence from small earthquakes in the Abruzzo region, Italy. *Geophysical Reseach Letters, 43*, 5000–5008.

Podvin, P., & Lecomte, I. (1991). Finite difference computation of traveltimes in very contrasted velocity models: a massively parallel approach and its associated tool. *Geophysical Journal International, 105*, 271–284.

Ruiz, J. A., Baumont, D., Bernard, P., & Berge-Thierry, C. (2011). Modeling directivity of strong ground motion with a fractal, k^{-2}, kinematic source model. *Geophysical Journal International, 186*, 226–244.

Sato, H., Fehler, M., & Maeda, T. (2012). *Seismic wave propagation and scattering in the heterogeneous earth structure* (2nd ed.). Berlin: Springer.

Schmedes, J., Archuleta, R. J., & Lavallée, D. (2010). Correlation of earthquake source parameters inferred from dynamic rupture simulations. *Journal Geophysical Research, 115*, B03304.

Somerville, P., Smith, N. F., Graves, W., & Abrahamson, N. (1997). Modification of empirical strong ground motion attenuation relations to include the amplitude and duration effects of rupture directivity. *Seismological Research Letters, 68*, 199–222.

Stidham, C., Antolik, M., Dreger, D., Larsen, S., & Romanowicz, B. (1999). Three-dimensional structure influences on the strong motion wavefield of the 1989 Loma Prieta earthquake. *Bulletin of the Seismological Society of America, 89*, 1184–1202.

Vyas, J Ch., Mai, P. M., & Galis, M. (2016). Distance and azimuthal dependence of ground-motion variability for unilateral strike-slip ruptures. *Bulletin of the Seismological Society of America, 106*,1584–1599.

Wei, S., Barbot, S., Graves, R., Lienkaemper, J. J., Wang, T., Hudnut, K., et al. (2015). The 2014 Mw 6.1 South Napa earthquake: a unilateral rupture with shallow asperity and rapid afterslip. *Seismological Research Letters, 86*, 344–354.

Zeng, Y., Anderson, J. G., & Yu, G. (1994). A composite source model for computing realistic synthetic strong ground motions. *Geophysical Reseach Letters, 21*, 725–728.

(Received July 29, 2016, revised October 5, 2016, accepted November 1, 2016, Published online November 14, 2016)